Insights into the Ochratoxin A/Aptamer Interactions on a Functionalized Silicon Surface by FTIR and UV–Vis Studies

Timothy Aschl, Gilles Frison, Anne Moraillon, Francois Ozanam, Philippe Allongue, Anne-Chantal Chantal Gouget-Laemmel

Insights into the ochratoxin A / aptamer interactions on a functionalized silicon surface by FTIR and UV-Vis studies

Timothy Aschl[1], Gilles Frison[2,3], Anne Moraillon[1], François Ozanam[1], Philippe Allongue[1*], Anne Chantal Gouget-Laemmel[1*]

[1] Laboratoire de Physique de la Matière Condensée, Ecole Polytechnique, CNRS, IP Paris, 91128 Palaiseau, France

[2] Laboratoire de Chimie Moléculaire, Ecole Polytechnique, CNRS, IP Paris, 91128 Palaiseau, France

[3] Laboratoire de Chimie Théorique, Sorbonne Université and CNRS, F-75005 Paris, France

[*] To whom correspondence should be addressed:
Anne-Chantal Gouget-Laemmel (anne-chantal.gouget@polytechnique.edu); Philippe Allongue (philippe.allongue@polytechnique.edu)

Abstract:

The association of a mycotoxin – ochratoxin A (OTA) – with a high-affinity DNA aptamer (anti-OTA) immobilized on a functionalized surface has been investigated at the molecular level. Anti-OTA aptamers are coupled by aminolysis in several steps on an acid-terminated alkyl monolayer grafted on a silicon substrate and Fourier-transform infrared (FTIR) spectroscopy in attenuated-total-reflection (ATR) geometry is used to assess the immobilization of anti-OTA (in its unfolded single-strand form) and determine its areal density (ca. 1.4 /nm^2). IR spectra further demonstrate that the OTA/anti-OTA association is efficient, selective and that several association/dissociation cycles may be conducted on the same surface. The areal density of OTA measured after association on the surface (IR spectroscopy) and after dissociation from the surface (UV-Vis spectroscopy) falls in the range 0.16 – 0.3 /nm^2 which is close to the areal density of a closed-packed monolayer of anti-OTA aptamers folded to form their G-quadruplex structure. The interactions between OTA and its aptamer at the surface are discussed with the help of DFT calculations – to identify the complex IR vibrational modes of OTA in solution – and UV-Vis spectroscopy – to determine the protonation state of the adsorbing species (i.e., OTA dissolved in the buffer solution) –.

Keywords: silicon surface; DNA aptamer; ochratoxin A OTA; quantitative FTIR spectroscopy; DFT calculation; UV-Vis spectroscopy

1. INTRODUCTION

Ochratoxin A (OTA) is one of the most widespread contaminants found in various food and feed such as cereals, coffee beans, dried fruits, wine or beer.[1,2,3] Produced by two fungi genera *Aspergillus* and *Penicillium*, this mycotoxin is severely toxic for humans, animals and plants, and therefore its fast detection in food samples is of prime importance to food safety, quality control and human health. **Figure 1** recalls the different protonation states of OTA according to the medium where it is dissolved. In its fully protonated form (1), OTA is composed of a chlorinated dihydroisocoumarin moiety which is amide-linked to L-phenylalanine. However, when the carboxylic acid group on C22 (pKa1 = 4.4) and the phenolic group on C9 (pKa2 = 7.3) deprotonate in physiological buffer, forms (2) and (3), respectively called OTA^- and OTA^{2-} in the following, co-exist. The existence of a fourth form corresponding to the ring-opened form of OTA (OP-OTA) is suggested at pH higher than 8-8.5[4,5] even though pH higher than 12 is necessary to hydrolyze the lactone ring.[6,7]

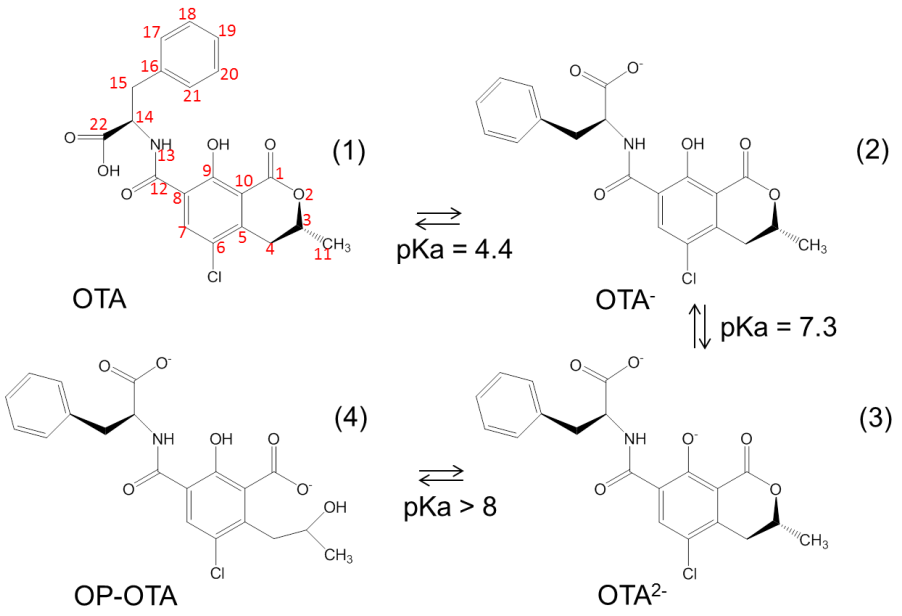

Figure 1. Chemical structures of OTA as a function of pH: acidic (1), close to neutral (2-3) and alkaline (4) media. Forms (1) to (4) are respectively designated in the text as OTA, OTA^-, OTA^{2-} and OP-OTA.

Mycotoxins such as OTA may be detected using biosensors [8,9,10,11,12] as it is a rapid and simple method with high specificity and sensitivity at relatively low cost compared to conventional chromatographic and immunoassay techniques.[13,14] In these devices, a specific probe is anchored on a solid surface to recognize the mycotoxin. In the case of OTA and various pathogens, particular attention has been given to aptamer-based biosensors, also called aptasensors.[15,16,17,18] Aptamers are single-stranded oligonucleotides (ssDNA) that bind with high specificity and affinity to a chemical or biological target.[19,20] They are synthesized in vitro by a selection procedure called Systematic Evolution of Ligands by EXponential enrichment (SELEX).[21] In addition, ssDNA may easily be modified with a suitable molecular linker to be anchored on a solid surface. Several aptamers against OTA were selected in buffers of pH ~7-7.4 and 8.5 with high binding affinities (association constants in the nM range).[22, 23, 24,25] Cruz-Aguado *et al.* established that aptamer 1.12.2 (called anti-OTA) presents a high affinity towards OTA.[22] It is composed of a sequence of 36 nucleotides with a high content of guanine (G) bases which fold into a G-quadruplex upon interaction with OTA, a structure commonly observed with DNA aptamers.[26,27] The anti-OTA aptamer is now commonly used as a probe because of its high affinity and its excellent selectivity towards OTA. In particular, it does not recognize compounds with similar structure such as N-acetylphenylalanine or warfarin and shows an affinity 100 times (fold) lower for ochratoxin B (OTB), the non-chlorinated analogue of OTA.[22]

Electrochemistry, colorimetric and fluorescence measurements were used to detect OTA – aptamer interactions.[17] Surface-Enhanced Raman Spectroscopy (SERS) has also proven to be a powerful technique to detect OTA with a very good sensitivity, in the micro to picomolar range.[28,29] Interestingly, these studies showed that the SERS spectrum after association with OTA on the surface was not the simple superposition of that of isolated OTA and that of isolated aptamer. A spectral signature of OTA could not be clearly assessed. In the

context of OTA detection, characterizing the association of OTA with anti-OTA aptamer immobilized on a solid support remains an important issue for a better understanding and the optimization of devices. To the best of our knowledge, such a characterization is still missing. The secondary structure of the aptamer–OTA complex was resolved in *solution* only by high resolution NMR spectroscopy[25] and circular dichroism.[26]

In this work, the surface association and dissociation of OTA with anti-OTA aptamer are studied at a molecular level using Fourier Transform IR (FTIR) spectroscopy in attenuated total reflection (ATR) geometry and UV-Vis measurement. DFT calculations are used to identify the complex IR vibrational modes of OTA at various protonation states. We stress that this study is a surface science study and it is not aiming at qualifying an aptasensor, though the results presented below might be considered as a premise to the design of such a Si-based device. The anti-OTA aptamer is immobilized by aminolysis on an acid-terminated alkyl monolayer grafted silicon surface taken as a model functionalized surface[30,31] (see scheme in **Fig. 2**). Quantitative IR spectroscopy is used to characterize the surface chemistry after each reaction step depicted in **Fig. 2**, in particular to determine the areal density of immobilized aptamers. The association of OTA on the surface, its selectivity and the possibility of performing several association / dissociation cycles are investigated in details. The areal density of associated OTA is quantitatively determined after calibration of the related IR intensity and after the dissociation of OTA from the surface by UV-Vis spectroscopy. The interactions between immobilized anti-OTA and surface OTA are discussed by comparing the spectra of *surface* OTA (after association) with that of OTA dissolved in solution.

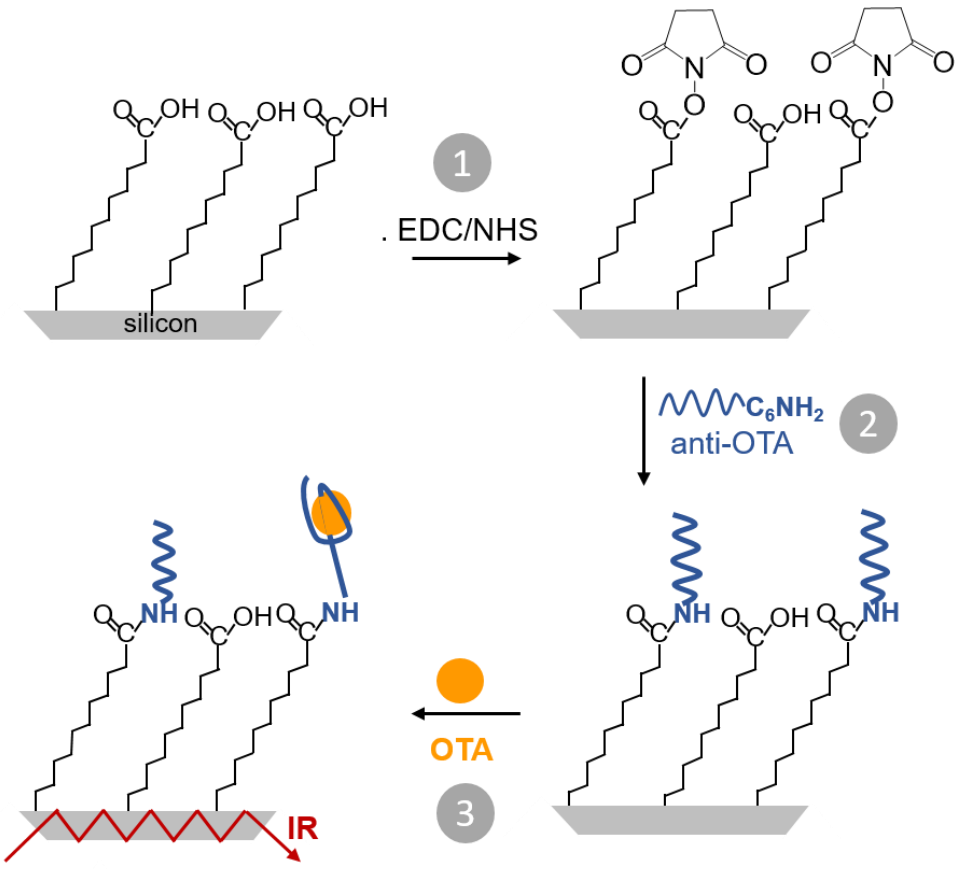

Figure 2. Schematic route to immobilize anti-OTA aptamer on a silicon surface functionalized with a COOH-terminated monolayer (steps 1-2) and schematic representation of the surface association OTA/anti-OTA (step 3).

2. EXPERIMENTAL

2.1. Materials

All cleaning (H_2O_2, 30%; H_2SO_4, 96%) and etching (HF, 50%) reagents were of RSE grade and were supplied by Carlo Erba. PBS 10X (Phosphate Buffered Saline, 1.37 M NaCl, 27 mM KCl, 0.1 M Na_2HPO_4, 18 mM KH_2PO_4) was purchased from Ambion and OTA from *Aspergillus ochraceus* from Sigma. Warfarin (analytical standard) was supplied by Fluka Analytical. TRIS (Tris(hydroxymethyl)aminomethane, molecular biology grade) was purchased from Research Organics, Tween20 was supplied by Calbiochem in Molecular Biology grade. All the other chemicals (undecylenic acid, N-hydroxysuccinimide NHS, 1-

ethyl-3-(3-dimethylaminopropyl) carbodiimide EDC), supplied by Sigma-Aldrich, were of the highest available grade and were used as received without further purification. Ultrapure water (UPW, Milli-Q, 18 MΩ cm) was used for the preparation of the solutions and for all rinses. The 36-mer aptamer anti-OTA (Eurogentec, France) was modified in 3' by an aminohexyl linker: 5'-GAT CGG GTG TGG GTG GCG TAA AGG GAG CAT CGG ACA-3'-C_6NH_2. The silicon samples were cut from double-side polished, float-zone purified, n-type, (111)-oriented, silicon wafers (Siltronix, France).

2.2. Preparation of OTA solutions

Solution for OTA association: A 34.7 mM ethanolic solution of OTA is prepared starting with OTA in dry state and mixed with the selected buffer to reach a final concentration of 1 mM OTA. The selected buffer composition is: 10 mM TRIS + 120 mM NaCl + 20 mM $CaCl_2$ + 5 mM KCl at pH 8.5.

Solution for OTA dissociation: The dissociation of OTA from the surface is conducted at 25°C in a regeneration buffer. The buffer composition consists of a 20/80 v/v mixture of methanol and a solution of 10 mM TRIS + 1 mM EDTA with a pH 9.

Solution for UV-Vis calibration in regeneration buffer. The OTA solutions were obtained by diluting the OTA stock solution (25 mM in H_2O, pH 8.5) in the regeneration buffer in order to get target concentrations between 1 µM and 0.05 µM.

2.3. Surface modification and OTA association / dissociation

Anti-OTA aptamers are immobilized in several steps on a functionalized silicon surface, shaped as an ATR prism. The as received Si(111) sample is cleaned in piranha solution at 100 °C for 30 min and copiously rinsed with UPW. Silicon oxide is then removed by a 5 s chemical etching in 50% HF, which leaves the surface H-terminated. The sample is quickly

rinsed in UPW and dried under nitrogen flow. *Safety considerations. The H_2SO_4/H_2O_2 (piranha) solution is a strong oxidant which reacts violently with organic materials. Hydrogen fluoride (HF) is a hazardous acid, which can result in serious tissue damage if burns are not appropriately treated. They must be handled with extreme care in a well-ventilated fume hood.*

The functionalization of the silicon surface with alkyl chains bearing COOH terminal groups (**Fig. 2**, top left) is obtained by photochemical hydrosilylation reaction between 1-undecylenic acid and the H-terminated Si surface.[32] The freshly etched sample is introduced in a Schlenk tube filled with neat oxygen-free undecylenic acid (which is previously outgassed at 100°C by bubbling Ar for 30 min, then cooled down at room temperature). After closing the tube, the photochemical reaction is conducted for 3 h in a UV reactor (wavelength 312 nm, 6 mW cm^{-2}). The sample is rinsed in hot acetic acid at 75°C (three times), to ensure that the surface is covered by a molecular monolayer, and dried under nitrogen flow. More experimental details are given in Reference[32].

The ester activated surface (step 1 in **Fig. 2**) is prepared by exposing the carboxy-terminated surface in a degassed aqueous solution containing 5 mM EDC + 5 mM NHS. The reaction lasts 1.5 h at a temperature of 17°C (controlled with a water bath) and the sample is rinsed with UPW and dried under nitrogen flow as detailed in Reference[33]. These experimental conditions ensure a reaction yield of 76% and leave a surface free of residues.

The anti-OTA is anchored on the previous surface (step 2 in **Fig. 2**) by aminolysis between the activated ester and the aminohexyl linker on 3' of the DNA strand. The reaction is conducted in a Schlenk tube filled with a 600 µM aptamer solution in a 150 mM phosphate buffer (NaH_2PO_4/Na_2HPO_4) with 0.01% SDS at pH 8.5 which is known to be efficient for this reaction.[35,36] The reactor is closed and left overnight. The sample is then sequentially rinsed for 1 min in PBS 1X, 10 min in PBS 1X + 0.1% SDS, 1 min in PBS 0.2X and 1 min in PBS

0.1X. A final rinse with UPW is applied before drying the sample in a stream of nitrogen gas. It is important to notice that, prior to aminolysis, the aptamer is *denatured*. Specifically, the aptamer solution is heated to 95°C for 5 minutes and cooled in ice for 10 minutes before it is transferred into a Schlenk tube (1 mL), which is kept at 25°C in a water bath and is purged with argon for 5 min before immersion of the NHS-terminated sample.

The OTA association on the aptamer-terminated surface (step 3 in **Fig. 2**) is conducted by immersing the sample in a Schlenk tube containing 1 mL of the selected buffer and kept at 25°C in a water bath. The solution for association is carefully purged with argon for 5 min before immersion of the silicon prism and again 5 min before the Schleck tube is closed. The sample is removed after 1 h and rinsed two times for 5 min with the selected buffer. After a final rinse in UPW the sample is blown-dried in a nitrogen-gas stream. For UV-Vis characterizations, OTA was dissociated from the surface by immersing the sample for 1 h in a controlled volume (1 mL) of the regeneration buffer at a temperature of 25°C. A final rinse in UPW is performed.

2.5. Surface Characterizations

Attenuated Total Reflection Fourier Transform Infrared (ATR-FTIR). ATR-FTIR spectra were recorded using a Bomem MB100 FTIR spectrometer coupled to a home-made, nitrogen-gas purged external ATR compartment, equipped with a liquid-nitrogen-cooled MCT photovoltaic detector. The spectra were successively collected for a p- and s-polarized IR beam. Standard spectra result from the accumulation of 100 scans with a 4 cm^{-1} resolution. In special cases (for the aptamer grafting and OTA detection), 9 accumulations of 100 scans were acquired to improve the signal-to-noise ratio. In this case the purge of the sample chamber was prolonged from 40 to 60 minutes to further minimize the influence of water vapor and carbon dioxide. Home-made crystalline silicon prisms were used as the ATR element. Their dimensions are typically 20 × 16 × 0.5 mm^3 with a number of reflections N ~

30 and a bevel angle of ~ 47°. The spectra were displayed as absorbance per reflection (computed using natural logarithm) by using a reference spectrum recorded prior to surface modification and then normalized to the actual number of reflections N. In-situ IR measurements were performed with a home-built PTFE cell of 0.5 mL volume.

UV-Vis spectroscopy. The UV-Vis measurements were accomplished with a Varian Carry 50 UV-Vis spectrophotometer. They were performed using glass cuvettes with an optical path length of 10 or 1 mm.

2.6. DFT calculation

Calculations were carried out with the Gaussian 09 package[37] and all structures were fully optimized without any symmetry constraints at the DFT level by means of the B3LYP functional.[38,39] The 6-31+G(d,p) basis set was applied for all atoms. Solvent effects are accounted for during the optimization process with the integral equation formalism version of the polarizable continuum model (IEFPCM) for methanol (OTA) or water (OTA^-, OTA^{2-} and OP-OTA). To get accurate geometries, the SCF convergence criterion was systematically tightened to 10^{-8} a.u., and the force minimizations were carried out until the rms force became smaller that (at least) 1×10^{-5} a.u. ("tight" optimization keyword in Gaussian 09). The "UltraFine" grid (99 radial shells and 590 angular points per shell) was used throughout the calculations, as recommended when using Gaussian 09. Harmonic vibrational frequency analysis, carried out to characterize the stationary points as local minima, was performed at the same level. Harmonic vibrational frequencies were uniformly scaled using a factor of 0.98[40] in the 1100-2000 cm^{-1} spectral range. Theoretical IR stick spectra are provided together with convoluted spectra obtained assuming a Gaussian profile with a width (fwhm) of 15 cm^{-1} in order to take into account the vibrational broadening in the liquid phase.

3. RESULTS AND DISCUSSION

3.1. Grafting of anti-OTA on silicon substrate

The immmobilization of anti-OTA aptamers on the functionalized silicon surface was conducted according to the scheme described in **Figure 2**. The p-polarized ATR-FTIR spectra of the same sample after each preparation step are displayed in **Figure 3** in the 1500-1900 cm^{-1} range. The hydrogen-teminated surface is used as a reference for all spectra. After hydrosilylation with undecylenic acid, spectrum (a) exhibits a νCO mode at 1717 cm^{-1} consistent with carboxylic acid end groups.[32] After activation with EDC/NHS (spectrum b), this IR band is replaced by a triplet band around 1788 cm^{-1} that is characteristic of the νCO mode of the succinimidyl group.[34] In the next step, the succinimidyl ester function is aminolyzed by immersing the sample in a buffer containing anti-OTA probes functionalized in 3' by an aminohexyl chain. A high concentration of anti-OTA (600 µM) is used to minimize the competition with hydrolysis[33] and four such activation/aminolysis cycles are conducted to maximize the amount of immobilized anti-OTA. The aptamer solution is heated prior to use in order to unfold possible bulky three-dimensional G-quadruplex structures. This step aims at performing the aminolysis reaction with single stranded oligonucleotides which maximizes the reaction yield (see experimental section for more details). After the 1st aminolysis, spectrum (c) presents a relatively weak amide I band at 1643 cm^{-1} together with a hardly discernible amide II band. The presence of a νCO mode (1728 cm^{-1}) suggests some back hydrolysis of the ester-NHS function during the aminolysis. After the 4th cycle (spectrum d), the intensity of the wide band at 1643 cm^{-1} has increased significantly while the νCO mode (1728 cm^{-1}) has vanished, though not entirely. This pertains to an increase of the amount of anti-OTA on the surface. The wide band at 1643 cm^{-1} may be assigned to guanines bases (17 against 6 thymine and 5 cytosine bases) that constitute the anti-OTA aptamer. Their contributions are in fact expected at wavenumbers lower than 1700 cm^{-1}.[41,42,43]

These p-pol spectra (and also s-pol spectra, data not shown) were analyzed to determine the surface composition and the final surface density of immobilized anti-OTA. The method requires a calibration experiment in order to convert the νCO and NHS band intensities into a surface density of COOH and NHS groups,[32, 33] as detailed in supporting information, **section S2**. The areal density of COOH and NHS groups per nm^2 is given in **Table 1**. After aminolysis, the areal density of anti-OTA is deduced from the intensity of the νCO band assigned to residual acid groups, assuming that the total density of grafted chains keeps constant throughout the entire process. After the 1st and 4th aminoloysis, the areal density of immobilized anti-OTA is estimated to be respectively 1.1 ± 0.2 and 1.4 ± 0.3 nm^{-2}. These densities are, within experimental uncertainty, smaller than the maximum packing density of ssDNA (the maximum packing density of $2/(d^2\sqrt{3})$ is in the range 1.2 – 3 per nm^2 knowing that the diameter of ssDNA is in the range d ~ 0.63[44] to ~ 1 nm [45]).

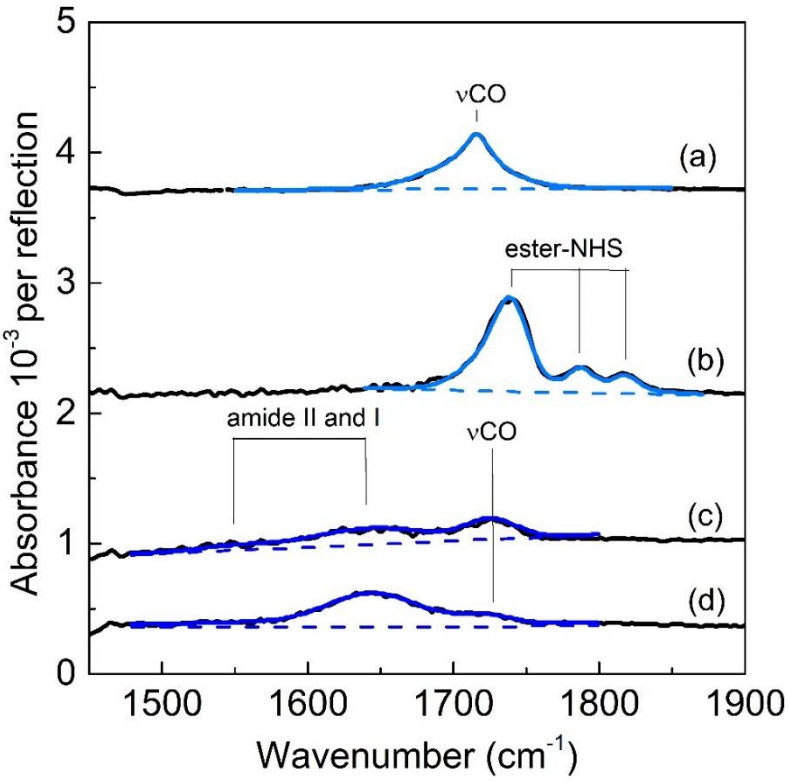

Figure 3. (a) ATR-FTIR spectra in p-polarization of the acid-terminated surface and after the successive steps of Fig. 2: (b) after EDC/NHS activation (step 1); (c) after aminolysis with

anti-OTA at 600 µM in a phosphate buffer (step 2); (d) after four activation/aminolysis cycles (step 3). The reference spectrum is that of the hydrogenated silicon surface. Solid blue lines are the envelop of the spectral analysis (see spectral decomposition in supplementary information, **Fig. S1**). The dashed line is the local baseline.

Table 1: Areal density of COOH and NHS groups determined from quantitative analysis of spectra in Fig. 3. The last two lines give the density of residual COOH and the last column the density of immobilized aptamers, assuming that the number of grafted chains stays constant throughout the whole protocol.

Surface state	COOH / nm^2	NHS / nm^2	Anti-OTA / nm^2
Acid monolayer (step 1)	1.7 ± 0.3		
Activated surface (step 2)	0.4 ± 0.08	1.3 ± 0.3	
1st aminolysis (step 3)	0.6 ± 0.1	-	1.1 ± 0.2
4th aminolysis	0.3 ± 0.06	-	1.4 ± 0.3

3.2. IR studies of OTA association / dissociation with surface anti-OTA

The "selected buffer" at pH 8.5 (SB) developed by Cruz-Aguado *et al.*[22] was used to study the OTA association on the surface. Another molecule called warfarin was used to check the selectivity of aptasensors against OTA since its chemical structure is close to that of OTA (see **Fig. S2**). **Figure 4**a shows the IR spectrum of the anti-OTA terminated surface sample exposed to a 1 mM warfarin solution in SB. The reference spectrum is that of the anti-OTA terminated Si surface (spectrum (d) of **Fig. 3**). Spectrum (a) is featureless, with no visible vibrational band in the 1300-1800 cm^{-1} range where warfarin presents well-defined and sharp IR bands (**Fig. S2**). This confirms that the aptamer-terminated surface has no or very little affinity towards warfarin.[22] By contrast, if a 1 mM OTA solution in selected buffer is used, a series of IR bands is resolved in the range 1400 – 1750 cm^{-1}, as shown in spectrum (b). These bands are however weak and their signature will be discussed in details later on. To check that this spectrum is actually characteristic of associated OTA in interaction with aptamers, the

sample was immersed in the regeneration buffer to dissociate OTA from the anti-OTA aptamer (see experimental section).[22] After 1 h of immersion, a featureless spectrum (c) is measured in the wavenumber range from 1450 to 1700 cm^{-1}. Spectrum (d) corresponds to the same sample exposed again to the OTA solution. It is quite similar to the spectrum (c) in the range 1450 cm^{-1} – 1700 cm^{-1}. The sole significant differences lie outside this spectral range. They consist of broad negative bands at 1716 cm^{-1} in spectra (c-d) and at 1410 cm^{-1} (spectrum c) or 1437 cm^{-1} (spectrum d), which are commented below.

All in all, the above spectral analysis indicates that the set of IR bands in the range 1475 et 1700 cm^{-1} is representative of *surface* OTA. After regeneration, there is an interference with a negative band between 1700 – 1750 cm^{-1} whose origin is briefly discussed below. To get rid of this interference, the quantification of associated OTA will be performed using spectrum (b) within the wavenumber range 1450 cm^{-1} – 1725 cm^{-1} (yellow shaded region) with the red baseline. This choice is justified in **section 3.4.** The data in **Figure 4** demonstrate further that (i) OTA association / dissociation with immobilized aptamers can be detected by IR spectroscopy; (ii) the association is selective since warfarin does not bind with anti-OTA; (iii) the anti-OTA terminated surface sustains a complete regeneration cycle, which is interesting for chemical sensing applications.

As noted above, the broad negative bands at 1716 cm^{-1} in spectra (c-d) and at 1410 cm^{-1} (spectrum c) or 1437 cm^{-1} (spectrum d) are interfering with the bands of surface OTA. They are tentatively assigned to the removal of residual acid chains because their positions are consitent with the vibration modes of acid chains:[32] (i) the band at 1716 cm^{-1} is readily assigned to the νC=O vibration of carboxyl groups; (ii) the second band which shifts from 1410 to 1437 cm^{-1} is tentatively assigned to overlaping in plane C-O-H (1410 cm^{-1}) and CH_2 scissor (1467 cm^{-1}) modes characteristic of linear saturated carboxylic acids. Under this hypothesis, we infer that a few physisorbed acid chains remaining on the as-prepared acid-

terminated surface are removed upon immersion of the sample in the alkaline buffer solutions used for association and dissociation. The loss is very small. It amounts to 0.1 acid chains/nm^2, which is negligible as compared to the initial acid chain density (1.7 chains/nm^2, see **Table 1**) and therefore does not affect the above analysis.

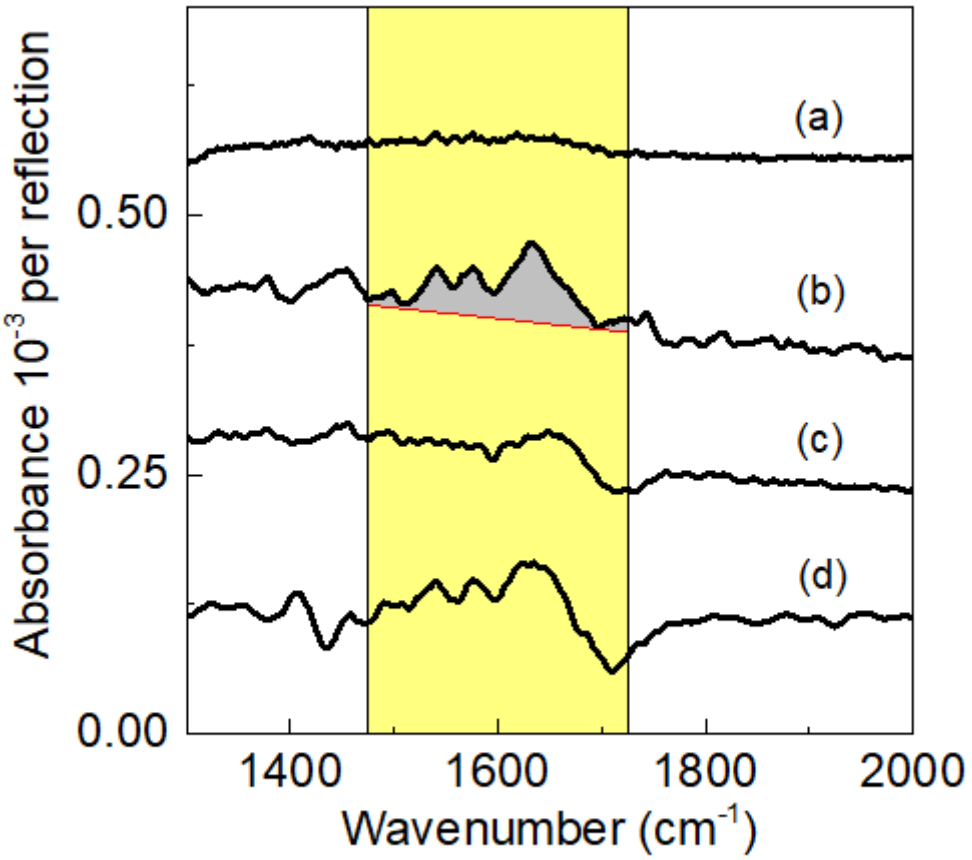

Figure 4: ATR-FTIR spectrum of a silicon sample with an anti-OTA terminated surface. The same sample is used to record the successive spectra. The reference spectrum is that of the anti-OTA terminated surface (spectrum (d) of **Fig. 3**). The plotted spectra are that of the sample (a) after 1 h exposition to 1 mM warfarin in the selected buffer; (b) after exposition to 1 mM OTA solution in the selected buffer; (c) after dissociation of OTA / anti-OTA duplex in the regeneration buffer of pH 9.5; (d) after a second association in 1 mM OTA solution. The yellow shaded region highlights the spectral range used for the quantification of the real density of OTA. The red line is the baseline used for the corresponding integration.

3.3. Conformation of associated OTA on the surface

This section aims at discussing the conformation of *surface* OTA, i.e., after association with the anti-OTA aptamer immobilized on the surface. **Figure A3** in Appendix 2 highlights that dissolved OTA presents a complex massif of IR bands in the range 1400-1750 cm^{-1} and that its exact shape depends on the protonation state of OTA. The assignment of the different IR bands of OTA was made possible with the help of DFT calculation (see also Tables **S1 to S3**) which reveals that several vibrational modes are extended coupled modes rather than localized ones.

Figure 5 recalls the spectrum of *surface* OTA after the 1^{st} association (spectrum a) and compares them with that of OTA^{2-} dissolved in a buffer at pH 8.5 (spectrum b). This comparison is justified because OTA^{2-} is the main species present in the selected buffer used for the association. The spectrum of protonated OTA in MeOH is also given for comparison (spectrum c). The general shape of spectrum (a) looks rather similar to that of spectrum (b) even though some subtle changes deserve a more detailed examination. The position of main IR bands of surface OTA is given in **Fig. 5**. The red marks are IR bands that may be considered as common to the spectrum of dissolved OTA^{2-} and OTA with a shift in position that is less than 20 cm^{-1}. The blue mark in (a) is an IR band that may be compared with that found in protonated OTA. The green marks are two bands which are present in OTA^{2-} but not in *surface* OTA. **Table 2** gives a list of all the above mentioned bands and their possible assignement.

The bands at 1540 cm^{-1} and ~1610 cm^{-1} are assigned to amide II and amide I bands , in view of their proximity to those recorded for dissolved OTA^{2-} (1530 cm^{-1} and 1635 cm^{-1}, respectively). The band at 1575 cm^{-1} is not far from the coupled mode [phenolate-ring deformation + νC_{12}=O amide, see Table S3] located at 1560 cm^{-1} in dissolved OTA^{2-}. The

band at 1460 cm^{-1} is also close to another complex coupled mode [phenolate-ring deformation + $\nu C_9–O^-$ phenolate, see Table S3] which is located at 1440 cm^{-1} in dissolved OTA^{2-}. The above coupled vibtational modes of OTA are consistently affected in terms of nominal frequency and amplitude by the molecular interaction between OTA^{2-} and anti-OTA aptamers. This is consitent with recent DFT calculation of the OTA-aptamer interactions[46,47] suggesting that OTA may interact via ionic bonds between the oxygen of the two carboxylate and Mg^{2+} ions from the selected buffer. Hydrogen bonds are also involved between the hydrogen of the amide and of the phenol ring with bases of the aptamers and between the three oxygen of the OTA (two from the carboxylate $C_{22}OO^-$ and the oxygen of the amide) with hydrogen of the central adenine base of the AAA motif (position 21) close to the G-rich part of the aptamer sequence responsible for binding to OTA. The red shift of the amide I band with respect to the peak in dissolved OTA^{2-} (1635 cm^{-1}) is also consistent with the presence of hydrogen bonding affecting the amide group.

It is nevertheless somewhat puzzling that the lactone mode is not clearly resolved in spectrum (a) whereas the $\nu C=O$ lactone (C_1) mode is a rather strong mode in dissolved OTA^{2-} and protonated OTA. It is inferred that the above mentioned non-covalent interactions (electrostatic interaction, hydrogen bonding and possibly other ones) can result in the shift and broadening of the lactone band. Its exact position is difficult to assess, which is depicted as the red shaded region in spectrum (a).

The band at 1740 cm^{-1} in spectrum (a) (blue bar) is a further difficult case. The presence of an acid-type νCO band in *surface* OTA is unexpected because it is obviously absent for OTA^{2-}. Because the frequency of this band (1740 cm^{-1}) is close to that of the acid group in protonated OTA (1725 cm^{-1}), it is inferred that the νCOO^- on C_{22} on OTA^{2-} is reprotonated upon association of OTA with the anti-OTA aptamer. This interpretation is supported by the absence of the two symmetric and antisymmetric elongation modes of

$C_{22}OO^-$ on dissolved OTA^{2-} (respectiveley at 1395 cm^{-1} and 1595 cm^{-1}, see green marks in spectrum (a) in **Fig. 5**).

The above discussion pertains therefore to the surface association of OTA^{2-} with the immobilized anti-OTA aptamer. The strong intermolecular interactions between OTA^{2-} and its host aptamer modify the delocalized vibrational modes and induce a partial reprotonation of OTA^{2-}.

Table 2: Frequency of main IR bands related to *surface* OTA and their possible assignements. The position and assigment of bands of dissolved OTA^{2-} (last column) are those of **Table S3**. The labelling of the carbon atoms refers to that shown in **Figure 1**.

Surface OTA	Assignment	Dissolved OTA^{2-}
1740 cm^{-1}	protonated $\nu C_{22}OOH$	*absent*
absent *absent*	$\nu_s C_{22}=OO^-$ $\nu_{as} C_{22}=OO^-$	1395 cm^{-1} 1595 cm^{-1}
Shoulder of band at 1610 cm^{-1}	$\nu C_1=O$ lactone	1685 cm^{-1}
1610 cm^{-1}	Amide I	1635 cm^{-1}
1540 cm^{-1}	Amide II	1530 cm^{-1}
1575 cm^{-1}	phenolate-ring deformation + $\nu C_{12}=O$ amide	1560 cm^{-1}
1460 cm^{-1}	phenolate-ring deformation + $\nu C_9–O^-$ phenolate	1440 cm^{-1}

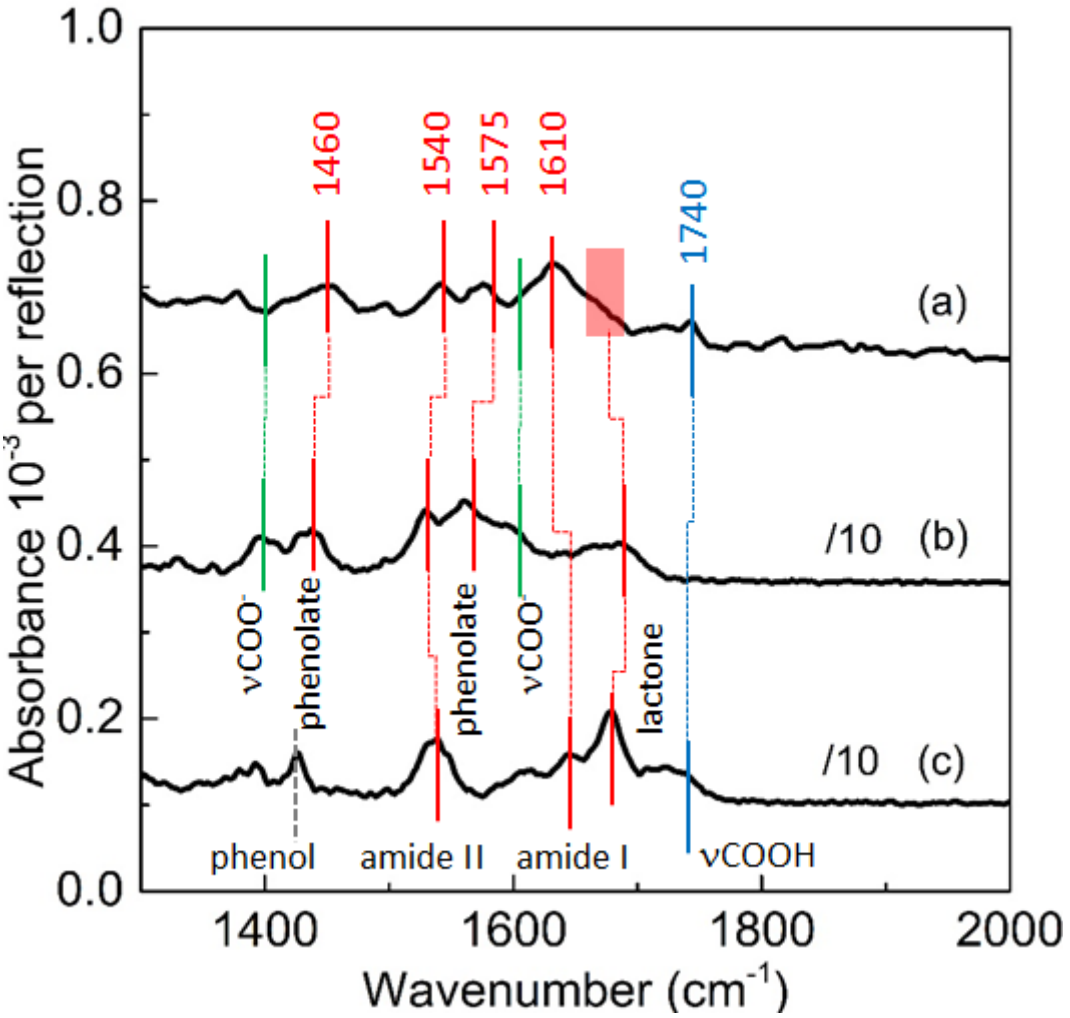

Figure 5: (a) ATR-FTIR spectra of OTA after the 1st association with the anti-OTA immobilized on the functionalized Si surface in the selected buffer. The reference spectrum is that of the anti-OTA terminated surface. (b) Spectrum of a 20 mM OTA^{2-} buffer solution of pH 8.5; (c) Spectrum of a 20 mM OTA solution in MeOH (protonated OTA). The position of IR bands of *surface* OTA is marked with vertical bars. Red marks are bands that are found in the spectra of OTA^{2-} and OTA in relevant solutions. The blue mark is a band that is found in *surface* OTA and protonated OTA only. Green marks are bands present in dissolved OTA^{2-} but absent in *surface* OTA.

3.4. Quantification of OTA association on the surface by UV-Vis

In this section, the areal density of surface OTA is quantified by two independent methods. In the first method, the IR intensity (s- and p-pol) assigned to surface OTA molecules is

integrated in the range 1475-1725 cm^{-1} (see yellow shaded region in **Fig. 4)**. Using this restricted range is justified because the lactone band of dissolved OTA^{2-} (see spectrum (b) in **Fig. 5**) is thought to be broadened and red-shifted in the spectrum of surface OTA (spectrum a, **Fig. 5**, see red box). It is then calibrated using the corresponding integrated absorbance of dissolved OTA^{2-} within the spectral range extending from amide II to lactone bands (see **Figure S3**) in an approach similar to the ones used to determine the number of COOH and ester-NHS vibrators. OTA^{2-} is considered because this is the species existing in the buffer used for association. Even though the spectra of surface and dissolved OTA^{2-} do not 100% match (see previous section), the analysis may yet be considered since differences consist of shifts and broadening of vibrations. This method gives an areal density of *surface* OTA of $0.16 \pm 0.05/nm^2$ (see **section S2** for more details of the quantification procedure and the IR calibration curve). The error is estimated to be within ~ 30%, if one includes the influence of the background determination.

The second method is complementary. OTA is dissociated from the surface (by immersion in a known volume (1 mL) of the regeneration buffer) and the solution is characterized by UV-Vis spectroscopy to determine its concentration. To increase the signal-to-noise ratio, 5 association / dissociation cycles are conducted so as to collect all OTA molecules within the same small volume of the regeneration buffer (1 mL). Here we exploit the fact that OTA may be associated and dissociated from the surface without significant alteration of the anti-OTA termination (**Fig. 4**). **Figure 6** shows the UV-Vis spectrum of the regeneration buffer after 5 cycles of association / dissociation. The absorption band around 380 nm is characteristic of dissolved OTA^{2-}, which was to be expected since the pH of the regeneration buffer solution is 9.5 (see **Fig. A1**). Using the calibration plot in **Fig. S4b**, the integrated absorption coefficient of the main band (0.364 nm cm^{-1}) corresponds to a concentration of 0.77 μM OTA^{2-}. Therefore, as detailed in **section S3** in the supporting

information, the areal density of associated OTA is 0.31 nm^{-2} by taking into account that the two faces of the prism have a surface of ca. 3 cm^2 and 5 cycles were conducted.

As noted above, the areal density of immobilized anti-OTA is as large as ~1.4 / nm^2 since precaution was taken to perform the aminolysis with *unfolded* single-stranded anti-OTA aptamers. Therefore, the yield of OTA association may look modest, with only 10-20 % of anchored anti-OTA capable of capturing a OTA molecule. However, one must account for the fact that upon OTA association, immobilized aptamers change of conformation, from unfolded ssDNA to ssDNA with a G-quadruplex structure. The bulky structure has a maximum close-packed areal density of only 0.22 – 0.4 nm^{-2} by considering a diameter of 1.69 – 2.3 nm for the G-quadruplex structure in comparable buffer solutions.[44] Therefore, finding an areal density of *surface* OTA of 0.16 - 0.3 /nm^{-2} is an excellent result since this value is quite close to the above mentioned density of 0.22 – 0.4 nm^{-2}. In other words, the capture of OTA by anti-OTA is limited by the steric hindrance of the G-quadruplex structures formed upon OTA capture and not by a surface-limited affinity of the aptamers. This demonstrates that the anchored anti-OTA keeps an excellent ability to bind with OTA^{2-}.

Previous studies demonstrated that the 3D structure of anti-OTA is promoted by the capture of OTA[26] while the 3D structure must be pre-existing for other systems (e.g. thrombin – binding aptamer).[48,49] This conclusion is consistent with the fact that OTA may be captured on a surface where the anti-OTA aptamers are immobilized as *unfolded* ssDNA. Upon regeneration the aptamer unfolds and it probably keeps this conformation because the second association is qualitatively as efficient as the first one without any specific treatment of the sample to unfold the attached aptamers.

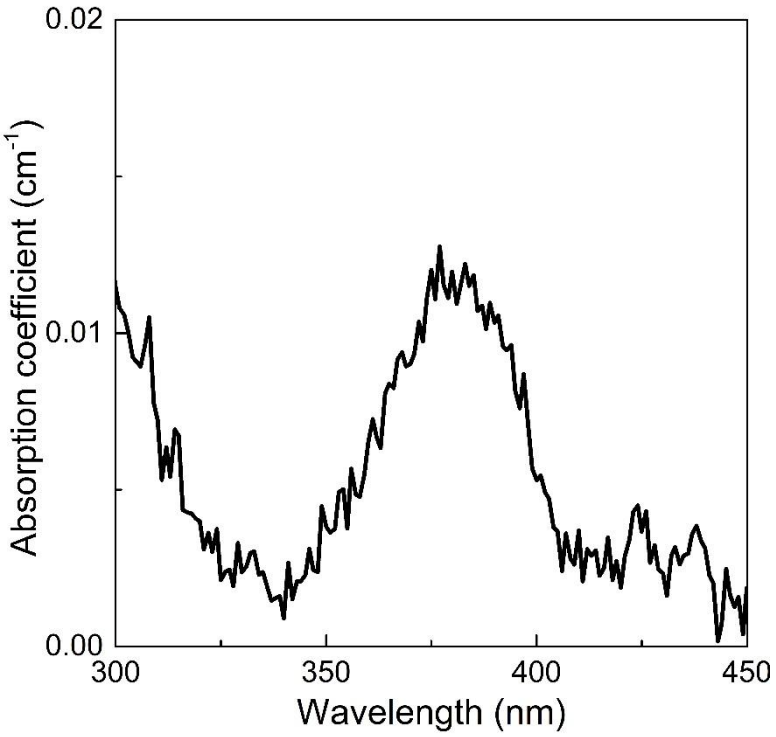

Figure 5. UV-Vis spectra of regeneration buffer of pH 9.5 after five cycles of association / dissociation of OTA from surface measured with a cuvette of optical path 1 mm. Note that the band at 380 nm is characteristic of OTA^{2-}. The integrated intensity is 0.364 nm cm^{-1}.

CONCLUSION

Anti-OTA aptamers modified with aminohexyl linker have been immobilized on a functionalized silicon substrate. The areal density of associated OTA is found to be in the range 0.16 – 0.3 /nm^2 from two independent methods and this value is very close to the areal density of a closed packed monolayer of anti-OTA aptamers with its bulky three-dimensional G-quadruplex structure (0.22 – 0.4 nm^{-2}). In other words, although the density of immobilized single stranded anti-OTA is 1.4 nm^{-2}, the surface keeps an excellent ability to associate with OTA from the solution since the final areal density of associated OTA is close to the maximum packing density of anti-OTA with its quadruplex structure. This is an important piece of information for biosensing applications. IR spectroscopy also evidences that the

associated OTA^{2-} is in strong interaction with its host aptamer because delocalized vibrational modes are greatly modified in terms of frequency and amplitude. A partial re-protonation of OTA^{2-} is also inferred. As a final note, the anti-OTA surface prepared in this work present properties relevant to biosensing applications: anti-OTA aptamer keeps its ability to bind with OTA^{2-} in spite of its immobilization on the surface; the surface is selective to OTA asssociation (warfarin does not bind) and may be reused since they withstand multiple association / dissociation cycles.

ACKNOWLEDGMENTS

T. A. thanks DGA for Ph.D. financial support.

APPENDIX A1: Characterization of OTA in solution by UV-Vis spectroscopy

UV-Vis spectra of OTA in methanol and in aqueous buffer solutions of $3 < pH < 11$ are shown in **Figure A1**. When OTA is fully protonated (in MeOH and at pH 3), the spectra show a single characteristic absorption band at 331 nm. Between pH 8.5 and 11, where OTA^{2-} is expected, the absorption band is now positioned at 379 nm and is also more intense. At intermediate pH, the band at 380 nm overlaps with a second band centered at 340 nm. The decrease in intensity of the 380 nm band is suggesting that di-anionic OTA^{2-} coexists with mono-anionic OTA^{-} in solution and that the band at 340 nm may be assigned to the later.[7] In strongly alkaline solution pH (14) there is a blue shift and a broadening of the 380 nm band, suggesting the coexistence of a second band at high energy (~350 nm). The interpretation of the later remains uncertain. It might be the result of the formation of OP-OTA by ring opening or to modified interactions between OTA^{2-} and molecular water at such a high pH. **Table A1** summarizes the band position of OTA as a function of its protonation state. Our results rule

out that the 380 nm band may be assigned to OP-OTA because it cannot form at pH < 11. This is in contrast with the interpretation of Bazin *et al.* [50]

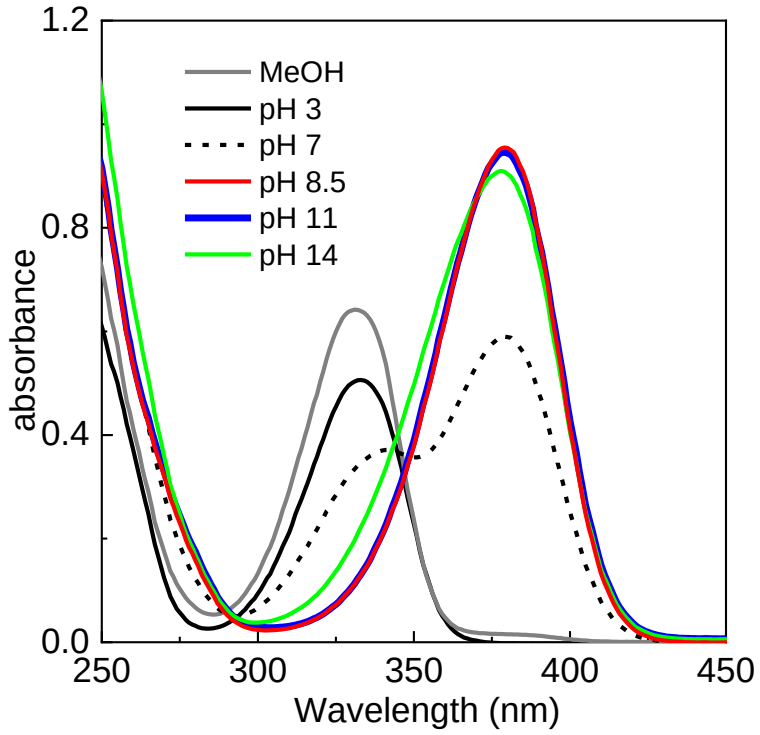

Figure A1. UV-Vis absorbance spectra of OTA (100 µM) dissolved in MeOH (grey) and in various aqueous buffer solutions: in citrate buffer at pH 3, in PBS 10X buffer at pH 7 and 8.5, in 10 mM NaOH at pH 11 and concentrated NaOH at pH 14, as indicted in the figure. In each case the pH was adjusted with HCl or NaOH solutions until the pH reached the desired value. The optical path is 1 cm.

Position (nm)	**OTA form**
331	**OTA**
340	**OTA^-**
380	**OTA^{2-}**

Table A1: Assignment of UV-Vis band to the different forms of OTA. No definitive assignment can be given for the band at 350 nm observed at pH 14 only. The structure of OTA species is given in **Fig. 1**.

APPENDIX A2: IR characterization of OTA in solution

This section compares the IR spectra of OTA dissolved in solution with calculated spectra (DFT calculation, see details in the experimental section) in order to assign the numerous bands observed experimentally (see Table S1-S4 in the supporting information). A concentration of 20 mM OTA solution was chosen to ensure that free OTA species are probed. An oxidized silicon prism in contact with the solution is used. Solutions of various pH are considered to study the protonation states of OTA.

As discussed in **Appendix A1**, OTA is fully protonated in methanol (form (1) in Fig. 1). **Figure A2** compares the calculated and experimental spectra of fully protonated OTA in methanol. Both spectra show strong similarity which allows an unambiguous assignment of the main vibrational peaks to be made, as already described by Bredenkam *et al.*[51] The assignments of the stretching mode of the carbonyl νCO from the carboxylic acid function at 1735 cm^{-1}, that from the lactone (coupled to the carbonyl of the amide) at 1654 cm^{-1} with a small contribution of the amide I mode at 1637 cm^{-1} are straightforward. The peaks at 1607 and at 1423 cm^{-1} are related to the phenol ring CC and COH vibrations and the last peak at 1536 cm^{-1} to the amide II vibration with intensity much higher than that of the amide I vibration. Below 1400 cm^{-1}, the major bands are assigned to the umbrella mode of methyl group $\delta_s CH_3$ at 1380 cm^{-1}, to the amide III and phenol vibrations at 1216 cm^{-1} and to the bending mode of the carboxylic acid group at 1148 cm^{-1}. In MeOH, the main differences as compared to the computed spectrum are the lower energy of νCO of the acid function at 1725 cm^{-1} and the presence of two distinct bands related to the νCO mode of the lactone at 1680 cm^{-1}, with a significant blue shift as compared to the computed spectrum, and to the amide I vibration at 1645 cm^{-1}, shifted to a much lower extent.

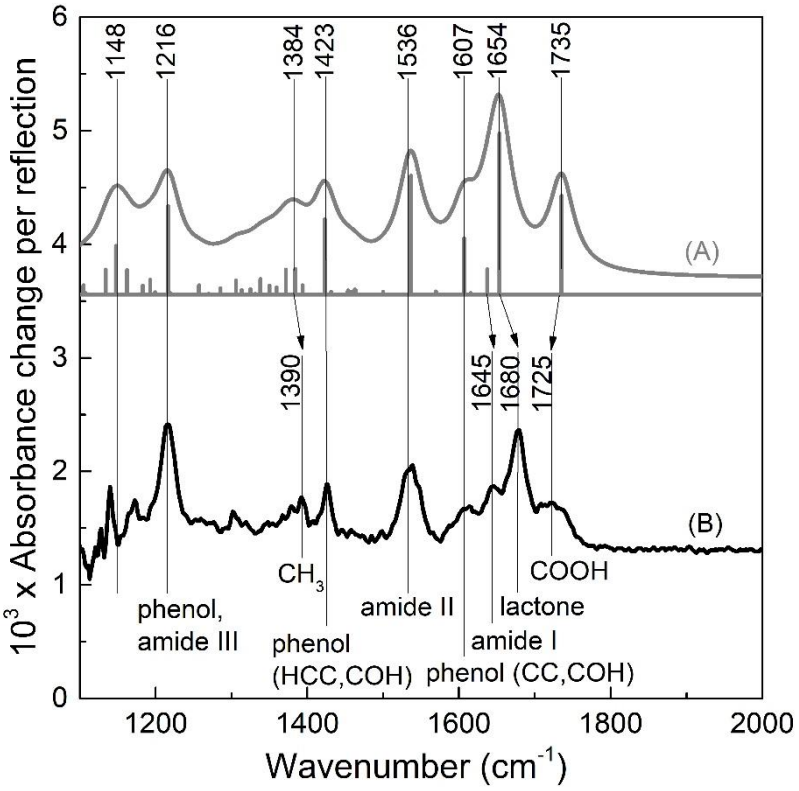

Figure A2: (A) Computed IR spectrum at the IEFPCM(MeOH)-B3LYP/6-31+G(d,p) level of protonated OTA (form (1)); (B) Experimental ATR-FTIR spectrum (ATR mode) in s-polarization of a 20 mM OTA solution in MeOH. The reference spectrum is that of pure methanol.

The top panel of **Fig. A3** displays the DFT calculated spectra of OTA^-, OTA^{2-} and OP-OTA. The three structures are characterized by the absence of the $\nu C_{22}O$ mode of the acid function at 1735 cm^{-1} and the presence of two asymmetric and symmetric $\nu C_{22}OO^-$ modes of the carboxylate around 1583 and 1362 cm^{-1}, respectively. For OTA^-, the other modes are not much affected as compared to the fully protonated form, the most noticeable difference being a shift of ~10 cm^{-1} to lower wavenumbers of the amide I and II vibrations. The spectrum of the di-anionic form OTA^{2-} exhibits more significant changes in the 1400-1700 cm^{-1} region as compared to OTA^- due to the rather strong vibrations of the phenolate ring at 1518 cm^{-1} and at 1465 cm^{-1} associated to the stretching mode of the C_9O^-. In parallel, the second deprotonation induces a strong shift of the νC_1O mode of the lactone at higher energy (up to 1675 cm^{-1}). In

the open-form OP-OTA, the peak related to the lactone disappears and a large band appears around 1445 cm^{-1} which stems from the deformation modes of the methyl group $\delta_a CH_3$ and other deformation modes of the hydroxylated alkyl chain of the open-form. **Figure A3-B** presents the experimental IR spectra of OTA dissolved in aqueous buffer solutions of pH 7, 8.5 and 11. As compared to the spectrum of OTA in methanol, the νC=O peak of the COOH group at 1715 cm^{-1} completely disappears when water is used as solvent at pH ≥ 7, evidencing the deprotonation of the OTA acid function. The spectra at pH 8.5 and 11 are identical (only one is shown in **Fig. A3-B**) and exhibit a roughly similar shape between 1360 and 1680 cm^{-1} when compared to that recorded at pH 7. In the spectra recorded at pH 8.5 or 11, the characteristic bands related to the νC_1O mode of the lactone at 1685 cm^{-1} and to the amide II and III vibrations at 1530 and 1195 cm^{-1} are present. Their positions are close to those of the calculated spectrum of OTA^{2-}. Contrary to DFT predictions, the amide I band around 1635 cm^{-1} overlaps the lactone band and the carboxylate modes are at higher wavenumber at 1395 and 1595 cm^{-1}. The phenolate-ring deformation modes are visible at 1560 and 1440 cm^{-1}. On the basis of the DFT-computed spectrum of OP-OTA, there is no evidence for the formation of the open-form at moderately alkaline pH, as also suggested by UV-Vis spectroscopy. From these results, we deduce that the toxin is under its di-anionic form OTA^{2-} at pH ≥ 8.5. Looking more closely at the differences in the spectra recorded at pH 7 and at pH 8.5 or 11, one notices the shift at lower energy of the νC=O mode of the lactone moiety and the presence of a new band related to the amide III, located at higher energy at 1219 cm^{-1}. On the basis of DFT calculations, these differences are clear indications that the mono-anionic OTA^- is formed together with OTA^{2-} at pH 7. Another clear-cut proof of the presence of OTA^- is the decrease of the phenolate bands associated to the broadening of two bands at 1425 and 1610 cm^{-1} resulting from the phenol ring and C-OH deformation. Even if the IR differences are less

obvious than those detected by UV-Vis spectroscopy, it appears clear that the two forms OTA^-/OTA^{2-} are present at pH 7.

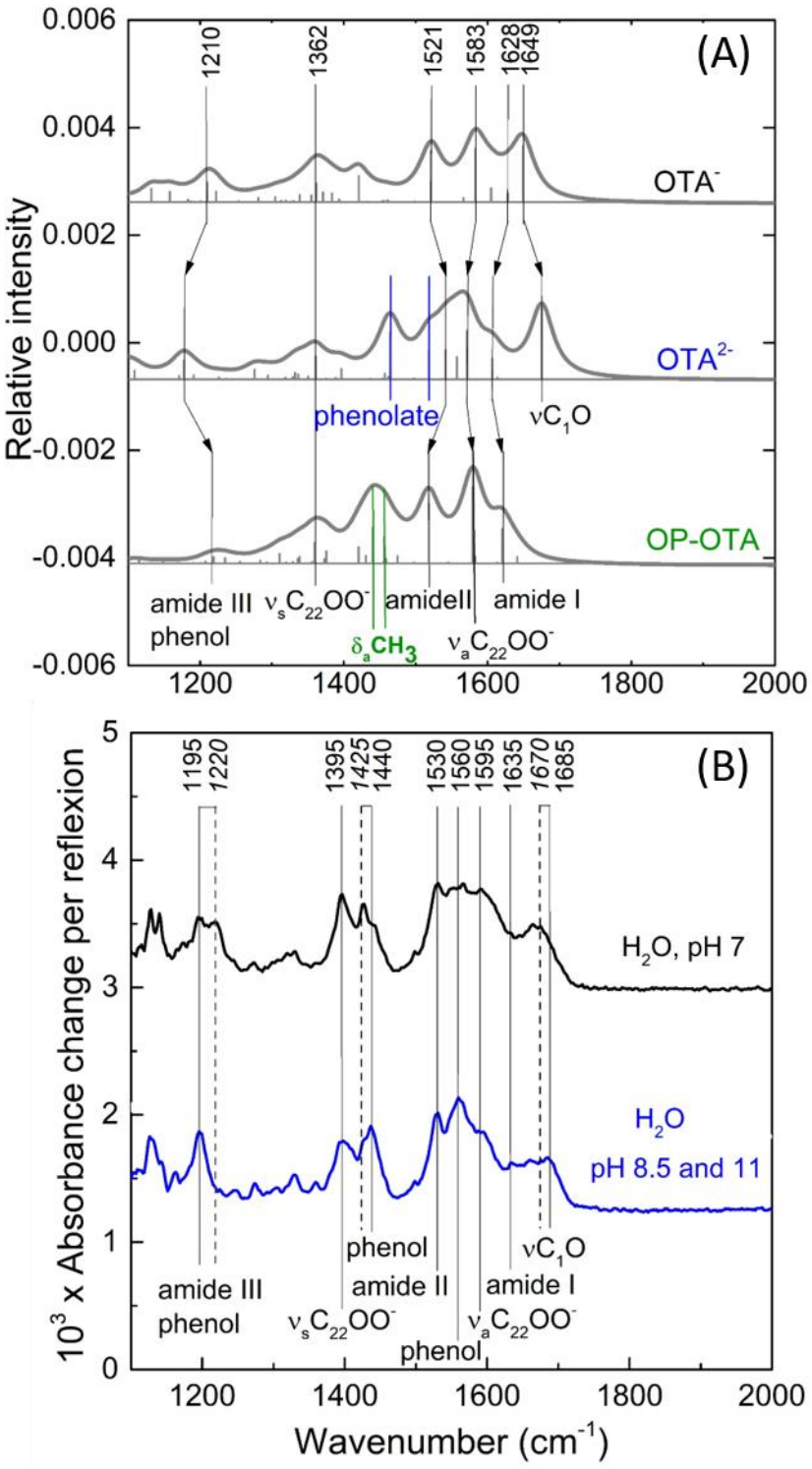

Figure A3: (A) Calculated IR spectra of OTA^-, OTA^{2-} and OP-OTA at the IEFPCM(H_2O)-B3LYP/6-31+G(d,p) level (B) Experimental ATR-FTIR spectra (s-polarization) of OTA

solutions of pH 7 and 8.5 to 11. The OTA concentration is 20 mM in ultrapure water and the pH is adjusted with NaOH. The reference spectrum is that of the OTA-free solution of same pH. The dashed lines in grey correspond to OTA^- vibrations observable at pH 7.

REFERENCES

1. Vanderme.Kj; Steyn, P. S.; Fourie, L.; Scott, D. B.; Theron, J. J., Ochratoxin A a toxic metabolite produced by aspergillus ochraceus wilh. *Nature* **1965,** *205* (4976), 1112-1113.
2. Pohland, A. E.; Nesheim, S.; Friedman, L., Ochratoxin A - A review (technical report). *Pure and Applied Chemistry* **1992,** *64* (7), 1029-1046.
3. Jorgensen, K., Occurrence of ochratoxin A in commodities and processed food - A review of EU occurrence data. *Food Additives and Contaminants Part a-Chemistry Analysis Control Exposure & Risk Assessment* **2005,** *22*, 26-30.
4. Dohnal, V.; Pavlikova, L.; Kuca, K., The pH and Mobile Phase Composition Effects Ochratoxin A Fluorescence at Liquid Chromatography. *Journal of Chromatographic Science* **2010,** *48* (9), 766-770.
5. Tozlovanu, M.; Pfohl-Leszkowicz, A., Ochratoxin A in Roasted Coffee from French Supermarkets and Transfer in Coffee Beverages: Comparison of Analysis Methods. *Toxins* **2010,** *2* (8), 1928-1942.
6. Xiao, H.; Madhyastha, S.; Marquardt, R. R.; Li, S. Z.; Vodela, J. K.; Frohlich, A. A.; Kemppainen, B. W., Toxicity of ochratoxin A, its opened lactone form and several of its analogs: Structure-activity relationships. *Toxicology and Applied Pharmacology* **1996,** *137* (2), 182-192.
7. Cagnasso, I.; Tonachini, G.; Berto, S.; Giacomino, A.; Mandrile, L.; Maranzana, A.; Durbiano, F., Comprehensive study on the degradation of ochratoxin A in water by spectroscopic techniques and DFT calculations. *RSC Adv.* **2019,** *9* (34), 19844-19854.
8. Prieto-Simon, B.; Campas, M.; Marty, J.-L.; Noguer, T., Novel highly-performing immunosensor-based strategy for ochratoxin A detection in wine samples. *Biosensors & Bioelectronics* **2008,** *23* (7), 995-1002.
9. Van Dorst, B.; Mehta, J.; Bekaert, K.; Rouah-Martin, E.; De Coen, W.; Dubruel, P.; Blust, R.; Robbens, J., Recent advances in recognition elements of food and environmental biosensors: A review. *Biosensors & Bioelectronics* **2010,** *26* (4), 1178-1194.
10. Rubab, M.; Shahbaz, H. M.; Olaimat, A. N.; Oh, D.-H., Biosensors for rapid and sensitive detection of Staphylococcus aureus in food. *Biosensors & Bioelectronics* **2018,** *105*, 49-57.
11. Vikesland, P. J.; Wigginton, K. R., Nanomaterial Enabled Biosensors for Pathogen Monitoring - A Review. *Environmental Science & Technology* **2010,** *44* (10), 3656-3669.
12. Lv, L. R.; Wang, X. Y., Recent Advances in Ochratoxin A Electrochemical Biosensors: Recognition Elements, Sensitization Technologies, and Their Applications. *Journal of Agricultural and Food Chemistry* **2020,** *68* (17), 4769-4787.
13. Turner, N. W.; Subrahmanyam, S.; Piletsky, S. A., Analytical methods for determination of mycotoxins: A review. *Analytica Chimica Acta* **2009,** *632* (2), 168-180.
14. Ha, T. H., Recent Advances for the Detection of Ochratoxin A. *Toxins* **2015,** *7* (12), 5276-5300.

15. Amaya-Gonzalez, S.; de-los-Santos-Alvarez, N.; Miranda-Ordieres, A. J.; Jesus Lobo-Castanon, M., Aptamer-Based Analysis: A Promising Alternative for Food Safety Control. *Sensors* **2013,** *13* (12), 16292-16311.
16. Song, K.-M.; Lee, S.; Ban, C., Aptamers and Their Biological Applications. *Sensors* **2012,** *12* (1), 612-631.
17. Rhouati, A.; Yang, C.; Hayat, A.; Marty, J.-L., Aptamers: A Promising Tool for Ochratoxin A Detection in Food Analysis. *Toxins* **2013,** *5* (11), 1988-2008.
18. Wang, J.; Li, G., Aptamers Against Cell Surface Receptors: Selection, Modification and Application. *Current Medicinal Chemistry* **2011,** *18* (27), 4107-4116.
19. Famulok, M.; Hartig, J. S.; Mayer, G., Functional aptamers and aptazymes in biotechnology, diagnostics, and therapy. *Chemical Reviews* **2007,** *107* (9), 3715-3743.
20. Jayasena, S. D., Aptamers: An emerging class of molecules that rival antibodies in diagnostics. *Clinical Chemistry* **1999,** *45* (9), 1628-1650.
21. Ellington, A. D.; Szostak, J. W., In vitro selection of RNA molecules that bind specific ligands *Nature* **1990,** *346* (6287), 818-822.
22. Cruz-Aguado, J. A.; Penner, G., Determination of Ochratoxin A with a DNA Aptamer. *Journal of Agricultural and Food Chemistry* **2008,** *56* (22), 10456-10461.
23. Barthelmebs, L.; Jonca, J.; Hayat, A.; Prieto-Simon, B.; Marty, J.-L., Enzyme-Linked Aptamer Assays (ELAAs), based on a competition format for a rapid and sensitive detection of Ochratoxin A in wine. *Food Control* **2011,** *22* (5), 737-743.
24. McKeague, M.; Velu, R.; Hill, K.; Bardoczy, V.; Meszaros, T.; DeRosa, M. C., Selection and Characterization of a Novel DNA Aptamer for Label-Free Fluorescence Biosensing of Ochratoxin A. *Toxins* **2014,** *6* (8), 2435-2452.
25. Xu, G. H.; Zhao, J. J.; Liu, N.; Yang, M. H.; Zhao, Q.; Li, C. G.; Liu, M. L., Structure-guided post-SELEX optimization of an ochratoxin A aptamer. *Nucleic Acids Research* **2019,** *47* (11), 5963-5972.
26. Yang, C.; Wang, Y.; Marty, J.-L.; Yang, X., Aptamer-based colorimetric biosensing of Ochratoxin A using unmodified gold nanoparticles indicator. *Biosensors & Bioelectronics* **2011,** *26* (5), 2724-2727.
27. Huizenga, D. E.; Szostak, J. W., A DNA aptamer that binds adenosine and ATP *Biochemistry* **1995,** *34* (2), 656-665.
28. Galarreta, B. C.; Tabatabaei, M.; Guieu, V.; Peyrin, E.; Lagugne-Labarthet, F., Microfluidic channel with embedded SERS 2D platform for the aptamer detection of ochratoxin A. *Analytical and Bioanalytical Chemistry* **2013,** *405* (5), 1613-1621.
29. Gillibert, R.; Triba, M. N.; de la Chapelle, M. L., Surface enhanced Raman scattering sensor for highly sensitive and selective detection of ochratoxin A. *Analyst* **2018,** *143* (1), 339-345.
30. Yang, J.; Chazalviel, J. N.; Siriwardena, A.; Boukherroub, R.; Ozanam, F.; Szunerits, S.; Gouget-Laemmel, A. C., A Quantitative Assessment of the Multivalent Protein-Carbohydrate Interactions on Silicon *Analytical Chemistry* **2014,** *86*, 10340-10349.
31. Yang, J.; Siriwardena, A.; Boukherroub, R.; Ozanam, F.; Szunerits, S.; Gouget-Laemmel, A. C., A quantitative method to discriminate between non-specific and specific lectin-glycan interactions on silicon-modified surfaces. *Journal of Colloid and Interface Science* **2016,** *464*, 198-205.
32. Faucheux, A.; Gouget-Laemmel, A. C.; Henry de Villeneuve, C.; Boukherroub, R.; Ozanam, F.; Allongue, P.; Chazalviel, J.-N., Well-defined carboxyl-terminated alkyl monolayers grafted onto H-Si(111): Packing density from a combined AFM and quantitative IR study. *Langmuir* **2006,** *22* (1), 153-162.

33. Moraillon, A.; Gouget-Laemmel, A. C.; Ozanam, F.; Chazalviel, J.-N., Amidation of monolayers on silicon in physiological buffers: A quantitative IR study. *J. Phys. Chem. C* **2008,** *112* (18), 7158-7167.
34. Sam, S.; Touahir, L.; Salvador Andresa, J.; Allongue, P.; Chazalviel, J.-N.; Gouget-Laemmel, A. C.; Henry de Villeneuve, C.; Moraillon, A.; Ozanam, F.; Gabouze, N.; Djebbar, S., Semiquantitative study of the EDC/NHS activation of acid terminal groups at modified porous silicon surfaces. *Langmuir* **2010,** *26*, 809-814.
35. Touahir, L.; Moraillon, A.; Allongue, P.; Chazalviel, J.-N.; Henry de Villeneuve, C.; Ozanam, F.; Solomon, I.; Gouget-Laemmel, A. C., Highly sensitive and reusable fluorescence microarrays based on hydrogenated amorphous silicon-carbon alloys. *Biosens. Bioelectron.* **2009,** *25* (4), 952-955.
36. Touahir, L.; Galopin, E.; Boukherroub, R.; Gouget-Laemmel, A. C.; Chazalviel, J. N.; Ozanam, F.; Szunerits, S., Localized surface plasmon-enhanced fluorescence spectroscopy for highly-sensitive real-time detection of DNA hybridization. *Biosensors & Bioelectronics* **2010,** *25* (12), 2579-2585.
37. Frisch, M. J. T., G. W.; Schlegel, H. B.; Scuseria, G. E.; Robb, M. A.; Cheeseman, J. R.; Scalmani, G.; Barone, V.; Mennucci, B.; Petersson, G. A.; Nakatsuji, H.; Caricato, M.; Li, X.; Hratchian, H. P.; Izmaylov, A. F.; Bloino, J.; Zheng, G.; Sonnenberg, J. L.; Hada, M.; Ehara, M.; Toyota, K.; Fukuda, R.; Hasegawa, J.; Ishida, M.; Nakajima, T.; Honda, Y.; Kitao, O.; Nakai, H.; Vreven, T.; Montgomery, J. A. Jr.; Peralta, J. E.; Ogliaro, F.; Bearpark, M.; Heyd, J. J.; Brothers, E.; Kudin, K. N.; Staroverov, V. N.; Kobayashi, R.; Normand, J.; Raghavachari, K.; Rendell, A.; Burant, J. C.; Iyengar, S. S.; Tomasi, J.; Cossi, M.; Rega, N.; Millam, J. M.; Klene, M.; Knox, J. E.; Cross, J. B.; Bakken, V.; Adamo, C.; Jaramillo, J.; Gomperts, R.; Stratmann, R. E.; Yazyev, O.; Austin, A. J.; Cammi, R.; Pomelli, C.; Ochterski, J. W.; Martin, R. L.; Morokuma, K.; Zakrzewski, V. G.; Voth, G. A.; Salvador, P.; Dannenberg, J. J.; Dapprich, S.; Daniels, A. D.; Farkas, O.; Foresman, J. B.; Ortiz, J. V.; Cioslowski, J.; Fox, D. J., *Gaussian, Inc., Wallingford CT, Gaussian 09* **2013**, Revision D.01

38. Becke, A. D., Density functional exchange energy approximation with correct asymptotic behavior *Physical Review A* **1988,** *38* (6), 3098-3100.
39. Lee, C. T.; Yang, W. T.; Parr, R. G., Development of the Colle-Salvetti correlation energy formula into a functional of the electron density *Physical Review B* **1988,** *37* (2), 785-789.
40. Katari, M.; Nicol, E.; Steinmetz, V.; van der Rest, G.; Carmichael, D.; Frison, G., Improved Infrared Spectra Prediction by DFT from a New Experimental Database. *Chemistry-a European Journal* **2017,** *23* (35), 8414-8423.
41. Nishimura, Y.; Morikawa, K.; Tsuboi, M., Infrared spectra of deoxyribonucleic acids with different base composition in their D_20 solutions *Bulletin of the Chemical Society of Japan* **1973,** *46* (12), 3891-3892.
42. Miyamoto, K. I.; Ishibashi, K. I.; Yamaguchi, R. T.; Kimura, Y.; Ishii, H.; Niwano, M., In situ observation of DNA hybridization and denaturation by surface infrared spectroscopy. *Journal of Applied Physics* **2006,** *99* (9).
43. Krummel, A. T.; Zanni, M. T., DNA vibrational coupling revealed with two-dimensional infrared spectroscopy: Insight into why vibrational spectroscopy is sensitive to DNA structure. *Journal of Physical Chemistry B* **2006,** *110* (28), 13991-14000.
44. Marsh, T. C.; Vesenka, J.; Henderson, E., A new DNA nanostructure, the G-wire, imaged by scanning probe microscopy *Nucleic Acids Research* **1995,** *23* (4), 696-700.
45. Hansma, H. G.; Revenko, I.; Kim, K.; Laney, D. E., Atomic Force Microscopy of Long and Short Double-Stranded, Single-Stranded and Triple-Stranded Nucleic Acids. *Nucleic Acids Research* **1996,** *24* (4), 713-720.

46. Motycka, J.; Mach, P.; Melichercik, M.; Urban, J., DFT and MD study of the divalent-cation-mediated interaction of ochratoxin A with DNA nucleosides. *Journal of Molecular Modeling* **2014,** *20* (6) 2274.
47. Phanchai, W.; Srikulwong, U.; Chompoosor, A.; Sakonsinsiri, C.; Puangmali, T., Insight into the Molecular Mechanisms of AuNP-Based Aptasensor for Colorimetric Detection: A Molecular Dynamics Approach. *Langmuir* **2018,** *34* (21), 6161-6169.
48. Baldrich, E.; Restrepo, A.; O'Sullivan, C. K., Aptasensor Development: Elucidation of Critical Parameters for Optimal Aptamer Performance. *Analytical Chemistry* **2004,** *76* (23), 7053-7063.
49. Nagatoishi, S.; Isono, N.; Tsumoto, K.; Sugimoto, N., Loop residues of thrombin-binding DNA aptamer impact G-quadruplex stability and thrombin binding. *Biochimie* **2011,** *93* (8), 1231-1238.
50. Bazin, I.; Faucet-Marquis, V.; Monje, M.-C.; El Khoury, M.; Marty, J.-L.; Pfohl-Leszkowicz, A., Impact of pH on the Stability and the Cross-Reactivity of Ochratoxin A and Citrinin. *Toxins* **2013,** *5* (12), 2324-2340.
51. Bredenkamp, M. W.; Dillen, J. L. M.; Vanrooyen, P. H.; Steyn, P. S., Crystal structures and conformational analysis of ochratoxin A and ochratoxin B- probing the chemical structure causing toxicity *Journal of the Chemical Society-Perkin Transactions 2* **1989,** (11), 1835-1839.

TOC